Supplement on *Quantifying methane emissions of the oil and gas sector in the Sultanate of Oman based on a helicopter-borne mass balance approach*

S1 Supplement to Introduction

Table S1. Overview of different methane (CH_4) inventories for O&G emission estimates.

Abbreviation	Full name	Reference
CAMS	Copernicus Atmosphere Monitoring Service (Global Anthropogenic Emissions)	Soulie et al. (2024)
CEDS	Community Emissions Data System	McDuffie et al. (2020)
Climate Watch	Climate Watch (WRI) – greenhouse gas & climate data platform	https://www.climatewatchdata.org
EDGAR	Emissions Database for Global Atmospheric Research	Crippa et al. (2018)
GFEI	Global Fuel Exploitation Inventory	Scarpelli et al. (2022)
IEA	International Energy Agency (Energy & Emissions Data)	https://www.iea.org/data-and-statistics

Table S2. CH_4 emission estimates from different inventories for the O&G sector worldwide, the Arabian Peninsula (AP) and for Oman.

Inventory	Year	World Mt CH_4 yr^{-1}	AP Mt CH_4 yr^{-1}	Oman kt CH_4 yr^{-1}	Sector description
CAMS-GLOB-ANT	2023	75	6.6	1083	fef_oil + fef_gas
CEDS	2023	75	8.9	2318	1B2_Fugitive-petr + 1B2b_Fugitive-NG-distr + 1B2b_Fugitive-NG-prod
Climate Watch	2022	88	7.2	678	Fugitive emissions
EDGAR_2025_GHG	2023	54	6.6	874	IPCC Code 2006: Oil and Natural Gas + Fossil Fuel Fires
GFEI	2020	32	2.2	237	Gas_All + Oil_All
IEA	2023	80	7.1	675	Gas pipelines and LNG facilities + Offshore gas (vented, fugitive) + Offshore oil (vented, flared, fugitive) + Onshore gas (vented, fugitive) + Onshore oil (vented, flared, fugitive) + Other from oil and gas + Satellite-detected large oil and gas emissions
Mean [range]		67 [32-88]	6.4 [2.2-8.9]	978 [237-2318]	

S2 Supplement to Methodology

This section provides supplementary methodological information for the MTG-Oman campaign. Section S2.1 summarises the campaign and instrumentation, including the complete *HELiPOD* flight programme and the sensors relevant for this study. Section S2.2 describes the derivation of an empirical quantification limit for the *HELiPOD* mass balance approach based on source-free upwind transects. It further presents applied weighting and bootstrap procedures, discusses underlying assumptions and limitations, and compares the resulting quantification limit with the controlled-release experiment of Förster et al. (2025).

S2.1 Campaign and instrumentation overview

Tables S3 and S4 provide the detailed campaign metadata and instrumental specifications underlying the analyses presented in this study. Table S3 summarises the complete *HELiPOD* flight programme, including flight timing, duration, number of MBEs, investigated regions and targets, and campaign-wide statistics, while Table S4 lists the measurement systems relevant for the CH_4 mass balance analysis together with their sampling rates and precisions. These details provide additional context for the temporal and spatial sampling coverage of the campaign and the instrumental basis of the emission estimates.

S2.2 Empirical quantification limit

This section describes the derivation of the empirical quantification limit for the *HELiPOD* mass balance approach. Section S2.2.1 introduces the concept and calculation of apparent null fluxes from source-free upwind transects, followed by the weighting and cluster-bootstrap approach in Sect. S2.2.2. The underlying assumptions and limitations are discussed in Sect. S2.2.3, while Sect. S2.2.4 presents the resulting null-flux distribution and quantification threshold. Finally, Sect. S2.2.5 compares the derived threshold with the controlled-release experiment of Förster et al. (2025).

S2.2.1 Concept and calculation of the empirical null flux

Following established approaches for deriving empirical detection thresholds from blank or source-free measurements (Currie, 1968, 1999; Hyslop and White, 2008), we estimated an empirical quantification limit of our airborne mass-balance approach by applying the flux calculation to source-free transects located upwind of the investigated facilities. In the absence of an emission source, the expected CH_4 flux enhancement is zero. Any non-zero flux calculated for these transects is therefore interpreted as an apparent or *null flux* caused by the combined effects of natural CH_4 variability, background determination, wind variability, measurement noise, and the assumptions of the flux calculation.

Suitable upwind transects were selected outside identifiable CH_4 plumes. Figure S1a shows an example of such a transect, including the measured CH_4 variability and horizontal wind vectors. Methane enhancements were determined using the same background approach as for the regular mass-balance experiments, with a linear background interpolated between the CH_4 mole fractions measured at the two edges of each transect (Fig. S1b and d). Both positive and negative enhancements were retained to avoid a systematic positive bias in the resulting null-flux distribution.

In contrast to the regular mass-balance experiments, which generally included several downwind transects at different altitudes and thus provided information about the vertical plume structure, the upwind data usually consisted of only one suitable transect at a single altitude. To obtain a first empirical estimate within the mass-balance framework, the measured CH_4 enhancement and perpendicular wind speed were therefore replicated vertically from the surface to the respective integration height (Fig. S1c and e). The resulting apparent flux was calculated as

$$\mathbf{Q_0} = \int_{\mathbf{s_1}}^{\mathbf{s_2}} \int_{\mathbf{0}}^{\mathbf{z_top}} \mathbf{\Delta c_{CH_4}(s,z)\, u_{\perp}(s,z)\, dz\ ds}, \tag{S1}$$

where Q_0 is the apparent CH_4 flux of the source-free transect, s is the horizontal coordinate along the transect, s_1 and s_2 define its lateral limits, z is altitude above ground, and ztop is the upper integration boundary. Furthermore, $\Delta cCH_4(s,z)$ denotes the CH_4 mass-concentration enhancement above background, and $u\perp(s,z)$ is the wind component perpendicular to the transect. The integrations over z and s represent the vertical and horizontal integration across the reconstructed curtain, respectively. The final integrated value across the complete transect was used as Q_0; variations in the cumulative flux along the transect reflect the spatial variability of CH_4 and wind (Fig. S1f).

Table S3. Summary of *HELiPOD* mission flights conducted during the METHANE-To-Go-Oman campaign between 14 November and 9 December 2023. For each flight, local flight time, duration, number of mass balance experiments (MBEs), measurement region, target number, source category (O&G – oil & gas) and type are listed. Regional summary rows provide the cumulative flight time, number of flights and MBEs, and the number of flights conducted for each target. The lower part of the table summarises campaign-wide flight statistics, including mean, minimum, and maximum flight duration, the distribution of flights by predominant flight period of the day, and the number of flights by source type. Morning, noon, and afternoon flights are defined as flights with more than 50 % of the flight time before 11:00 local time (LT), between 11:00 and 14:00 LT, and after 14:00 LT, respectively. B.L denotes the landfill measurement area near Region B. One flight in Region C yielded no usable data.

Date	Flight	Time (LT)	Duration	MBEs	Region	Target	Source	Type
2023-11-14 /Tue	F01	10:40-13:15	2h 35 min	2	A	1	O&G	Sweet
2023-11-15 /Wed	F02	08:45-11:15	2h 30 min	2	A	2	O&G	Sweet
2023-11-16a /Thu	F03	08:45-11:35	2h 50 min	2	A	1	O&G	Sweet
2023-11-16b /Thu	F04	14:35-17:00	2h 25 min	2	A	1	O&G	Sweet
2023-11-17 /Fri	F05	09:00-11:15	2h 15 min	2	A	2	O&G	Sweet
2023-11-18 /Sat	F06	09:00-11:45	2h 45 min	2	A	2	O&G	Sweet
Flight hours			15 h 20 min		Target 1	3 flights		
Flights	6		MBEs	12	Target 2	3 flights		
2023-11-21 /Tue	F07	14:25-16:55	2h 30 min	1	B	3	O&G	Sweet
2023-11-23a /Thu	F08	10:20-12:40	2h 20 min	2	B	4	O&G	Sweet
2023-11-23b /Thu	F09	14:45-16:50	2h 05 min	1	B	4	O&G	Sweet
2023-11-24a /Fri	F10	08:30-11:05	2h 35 min	1	B	3	O&G	Sweet
2023-11-24b /Fri	F11	14:20-16:55	2h 35 min	1	B	3	O&G	Sweet
2023-11-25 /Sat	F12	08:15-11:05	2h 50 min	3	B	4	O&G	Sweet
2023-11-26 /Sun	F13	15:00-17:20	2h 20 min	1	B	3	O&G	Sweet
Flight hours			17 h 15 min		Target 3	4 flights		
Flights	7		MBEs	10	Target 4	3 flights		
2023-11-27a /Mon	F14	08:15-10:35	2h 20 min	1	B.L	L	waste	landfill
2023-11-27b /Mon	F15	14:40-17:30	2h 50 min	1	B.L	L	waste	landfill
2023-11-28a /Tue	F16	08:15-10:45	2h 30 min	2	B.L	L	waste	landfill
2023-11-28b /Tue	F17	14:15-17:00	2h 45 min	2	B.L	L	waste	landfill
Flight hours			10 h 25 min		Target L	4 flights		
Flights	4		MBEs	6				
2023-12-05a /Tue	F18	08:15-10:55	2h 40 min	1	C	5	O&G	Sour
2023-12-05b /Tue	F19	14:55-17:05	2h 10 min	1	C	5	O&G	Sour
2023-12-06 /Wed	F20	08:15-11:00	2h 45 min	2	C	6	O&G	Sour
2023-12-07a /Thu	F21	08:15-11:00	2h 45 min			no data available		
2023-12-07b /Thu	F22	14:30-16:55	2h 25 min	2	C	6	O&G	Sour
2023-12-08a /Fri	F23	08:00-10:40	2h 40 min	1	C	6	O&G	Sour
2023-12-08b /Fri	F24	13:50-16:35	2h 45 min	2	C	6	O&G	Sour
2023-12-09a /Sat	F25	08:00-10:05	2h 05 min	2	C	5	O&G	Sour
2023-12-09b /Sat	F26	13:55-16:10	2h 15 min	2	C	6	O&G	Sour
Flight hours			22 h 30 min		Target 5	3 flights		
Flights	9		MBEs	13	Target 6	5 flights		

Flight statistics			
Mean	2 h 31 min		
Minimum	2 h 05 min		
Maximum	2 h 50 min		
Morning flights	13	before 11:00 LT	
Noon flights	2	between 11:00 and 14:00 LT	
Afternoon flights	11	after 14:00 LT	
Sweet O&G			13
Sour O&G			8
Landfill / waste			4
No usable data			1

	Flights	Duration	MBEs	Regions	Targets
Sum	26	65 h 30 min	41	3	7

Table S4. Overview of the *HELiPOD* sensors relevant for this study.

Instrument	Species/Parameter	Data rate	Precision
Picarro G2401-m	CH_4 & CO_2	~ 2 Hz	~ 2 ppb
Cavity ringdown spectroscopy (CRDS)			
Licor LI-7700	CH_4	40 Hz	~ 5 ppb @ 10 Hz
Open path gas analyser			
Meteorological sensors	Wind vector	100 Hz	0.1 m s^{-1}, 3°
	Temperature	100 Hz	0.1 K
	Humidity	100 Hz	1 % RH

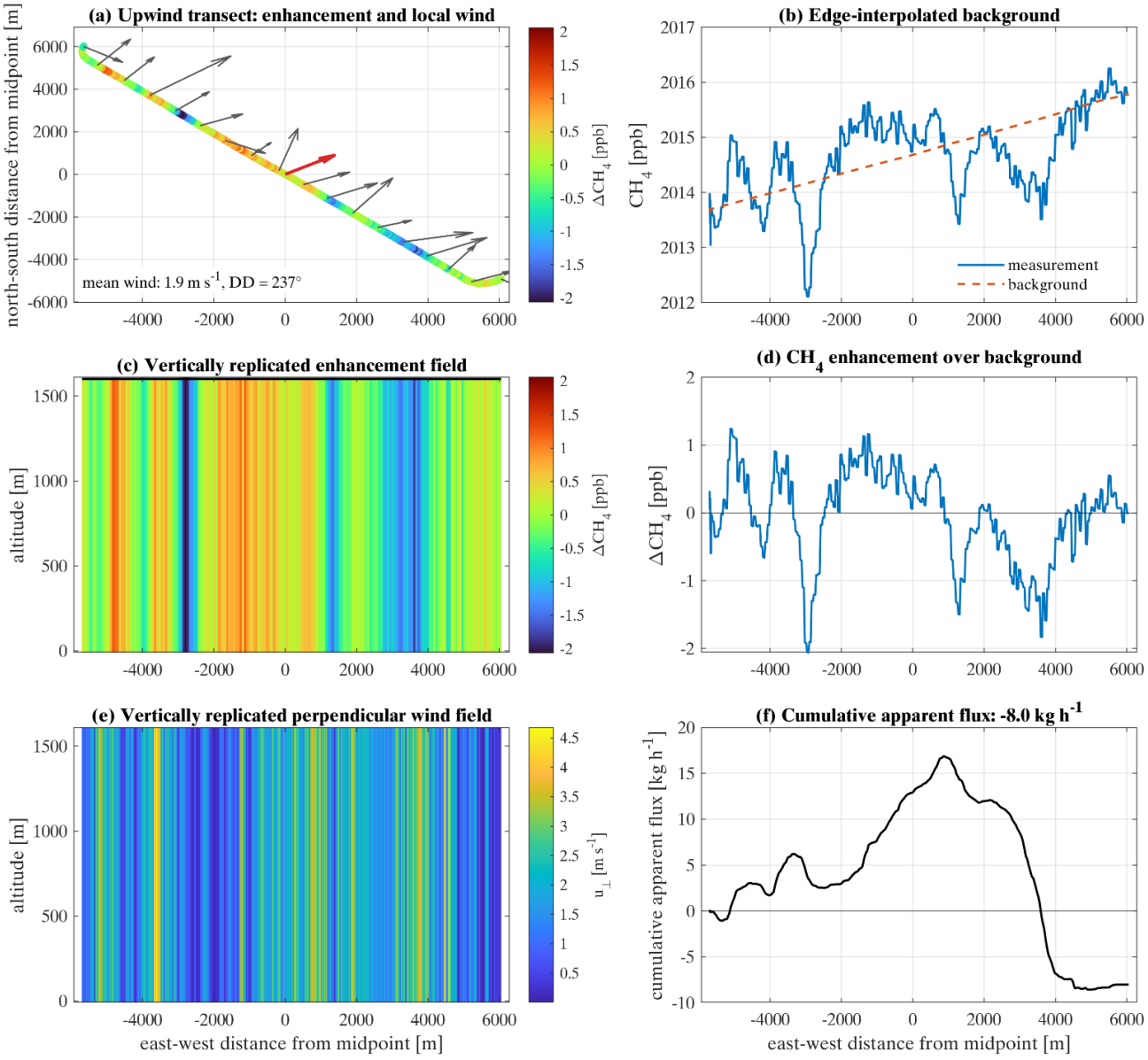


Figure S1. Illustration of the apparent CH_4-flux calculation for a source-free upwind transect. The example shows the transect C1 to D1 from Flight F11 on 24 November 2023. (a) Flight path coloured by the CH_4 enhancement relative to the background. Grey arrows indicate the local horizontal wind, and the red arrow shows the mean wind. (b) Measured CH_4 mole fraction along the transect and the background determined from the transect edges. (c) Background-corrected CH_4 enhancement vertically replicated from the surface to the upper integration boundary. (d) One-dimensional CH_4 enhancement along the transect, including both positive and negative values. (e) Wind component perpendicular to the transect, vertically replicated over the same integration layer. (f) Cumulative apparent CH_4 flux obtained by integrating the product of CH_4 mass-concentration enhancement and perpendicular wind speed. The final value across the complete transect represents the apparent null flux Q_0.

This procedure was applied to 71 source-free transects obtained during 22 flights. The resulting signed apparent fluxes form an empirical null-flux distribution representing the variability of the complete calculation method under campaign conditions. Its positive 95th percentile, Q_{95}, was used as the empirical quantification threshold, following the established concept of defining a detection threshold from the upper 95th percentile of blank or source-free measurements (Hyslop and White, 2008). Under the null hypothesis that no source is present, 95 % of the apparent fluxes are expected to remain below this value, whereas only 5 % exceed it. Thus, a measured flux above Q_{95} is unlikely to result from the variability represented by the null measurements alone. However, this does not prove the existence of a source by itself and should be supported by a coherent plume structure and, where possible, repeated measurements.

S2.2.2 Weighting and bootstrap approach

Since the number of suitable upwind transects differed among flights, two weighting approaches were applied. In the transect-weighted distribution, every transect contributed equally, meaning that flights containing several transects had a greater influence on the result. In the equal-flight-weighted distribution, each flight contributed the same total weight, independent of the number of available transects. The latter reduces the dominance of individual, more extensively sampled flights and gives equal importance to the atmospheric conditions encountered during each flight.

The sampling uncertainty of Q_{95} was assessed using a cluster bootstrap in which entire flights were resampled. For each bootstrap iteration, 22 flights were randomly drawn from the original dataset, whereby individual flights could be selected more than once while others were omitted. All transects belonging to a selected flight were retained together. The 95th percentile was recalculated for each resampled dataset. The resulting bootstrap confidence interval describes the sensitivity of the estimated threshold to the limited set of sampled flights rather than an additional instrumental or measurement uncertainty.

S2.2.3 Applicability, assumptions, and limitations

The approach provides an empirical end-to-end assessment because the upwind transects were measured with the same platform and instrumentation and processed using the same background and flux-calculation framework as the regular mass-balance experiments. The resulting distribution therefore incorporates several interacting contributions that cannot be represented by analyser precision alone, including:

- natural spatial CH_4 variability;
- uncertainty in the background determination;
- variability in wind speed and direction;
- covariance between CH_4 and wind fluctuations;
- flight-path and sampling effects;
- assumptions concerning the vertical integration.

The vertical replication is a simplified approximation and differs from the regular mass-balance experiments, for which measurements at several altitudes provide information about the vertical distributions of both CH_4 and wind. For the present purpose, replicating the CH_4 variability is considered acceptable because the analysis is intended to quantify how naturally occurring horizontal concentration fluctuations propagate through the flux calculation rather than to reconstruct a physical upwind concentration profile.

Replicating the wind field introduces greater uncertainty because wind speed and direction may change with altitude. The approximation assumes that the wind within the investigated boundary layer does not vary sufficiently strongly to fundamentally change the order of magnitude of the resulting null fluxes. This is broadly supported by the available vertical

measurements during the campaign, although stronger vertical gradients may occur, particularly during the development or decay of the boundary layer. Future applications could reduce this uncertainty by collecting source-free transects at several altitudes.

The derived threshold remains limited by the relatively small number of independent flights. Although 71 transects were analysed, several were obtained during the same flight and therefore do not represent independent meteorological conditions. This limited sampling is also reflected in the relatively broad bootstrap confidence intervals. In addition, the method is inherently campaign-specific: the null-flux distribution depends on the encountered atmospheric variability, wind conditions, boundary-layer depth, integration height, and flight strategy. The resulting value should therefore be interpreted as a coarse empirical estimate rather than as a universal detection limit of the *HELiPOD* or the mass-balance method.

S2.2.4 Empirical null-flux distribution and quantification threshold

The 71 source-free upwind transects produced signed apparent CH_4 fluxes on both sides of zero, ranging approximately from −13 to +16 kg h^{-1} (Fig. S2a). The median of the all-transect distribution was 0.01 kg h^{-1}, while the weighted median of the equal-flight-weighted distribution was −0.07 kg h^{-1}. Both values are close to zero, as expected for source-free measurements, and indicate no systematic positive bias in the null-flux calculation.

The choice of weighting affected the shape of the empirical distribution and, consequently, the estimated empirical quantification threshold (Fig. S2b and c). When all transects were weighted equally, the positive 95th percentile was

$$Q_{95,\mathrm{transect}} = 6.3\ \mathrm{kg\,h^{-1}}$$

with a cluster-bootstrap 95 % confidence interval of

$$95\ \%\ \mathrm{CI}: 3.2 – 15.6\ \mathrm{kg\,h^{-1}}$$

Assigning equal total weight to each of the 22 flights resulted in

$$Q_{95,\mathrm{flight}} = 11.2\ \mathrm{kg}\ h^{-1}$$

with a cluster-bootstrap 95 % confidence interval of

$$95\ \%\ \mathrm{CI}: 3.3 – 15.6\ \mathrm{kg\,h^{-1}}$$

The higher equal-flight-weighted value results from relatively large positive apparent fluxes during some flights with only a few suitable transects, whereas flights with numerous transects generally showed considerably smaller null fluxes and dominated the transect-weighted distribution. Since the equal-flight-weighted approach better represents the variability among different flights and meteorological conditions, its value of approximately 11 kg h^{-1} is used as the mean campaign-specific estimate of the empirical quantification limit.

The broad bootstrap interval reflects the limited number of independent flight conditions and the sensitivity of an upper percentile to individual flights. The lower confidence bound does not represent a lower quantification threshold; instead, it indicates that the estimated Q_{95} could be smaller for a different composition of the limited flight sample. Likewise, the upper confidence bound quantifies the extent to which the estimated threshold could increase under resampling of the available flights.

Accordingly, 11 kg h^{-1} is retained as the mean empirical estimate, while the upper cluster-bootstrap confidence limit of approximately 16 kg h^{-1} is used as a conservative quantification threshold for interpreting small flux estimates. Fluxes below or near this conservative threshold may be difficult to distinguish robustly from the variability represented by the null measurements. Fluxes exceeding this conservative threshold are unlikely to originate from methodological variability alone

and are therefore likely to represent real emissions. Estimates only slightly above the threshold should nevertheless be validated by a spatially coherent plume and, where possible, repeated independent mass-balance measurements.

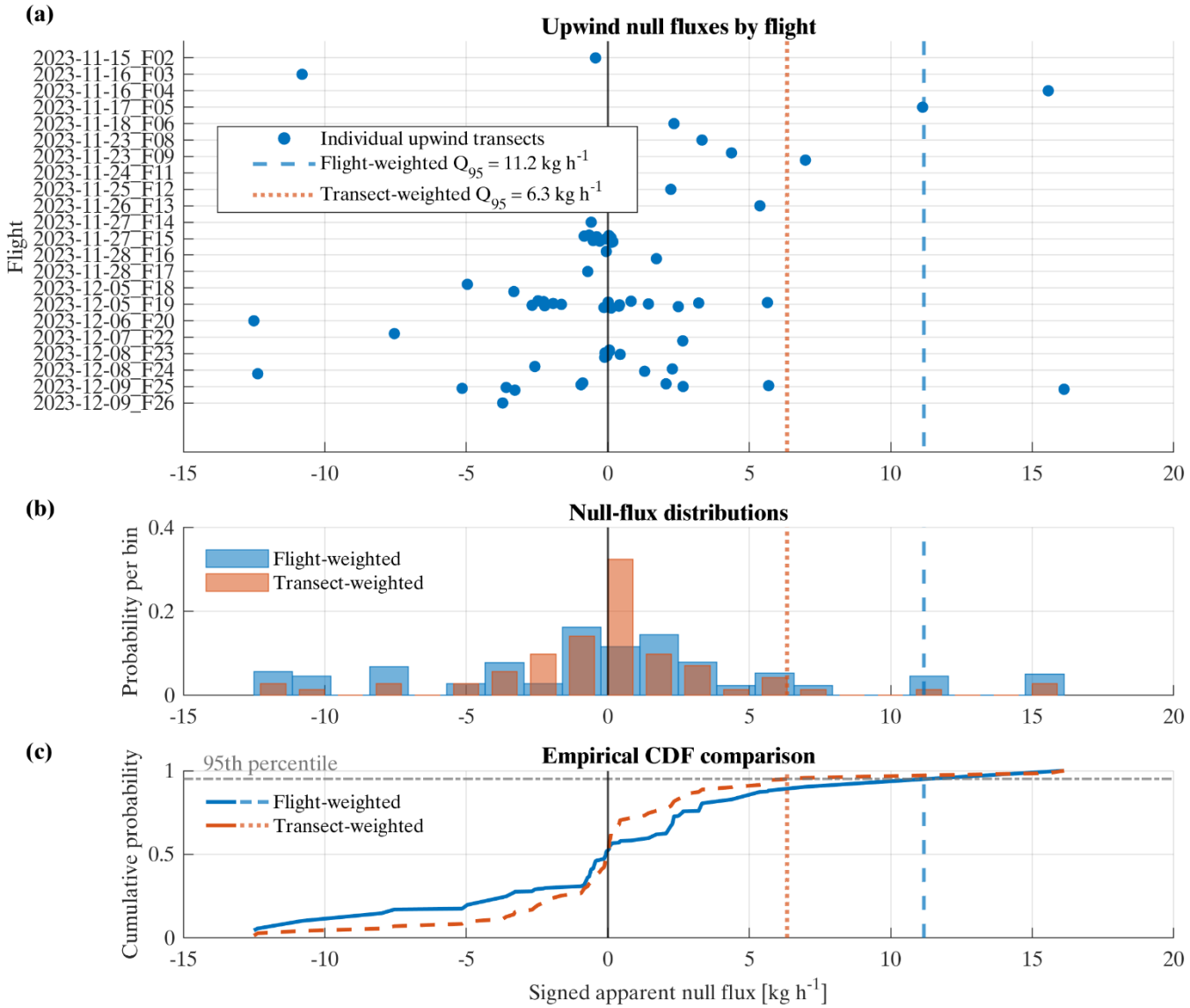


Figure S2. Empirical null-flux distributions derived from source-free upwind transects. (a) Signed apparent CH_4 fluxes calculated for 71 upwind transects obtained during 22 flights. The black vertical line marks zero flux. The orange dotted and blue dashed lines denote the transect-weighted and equal-flight-weighted positive 95th percentiles of 6.3 and 11.2 kg h^{-1}, respectively. (b) Probability histograms of the transect-weighted and equal-flight-weighted distributions. In the former, all transects contribute equally, whereas in the latter each flight contributes the same total weight. (c) Corresponding empirical cumulative distribution functions. The horizontal grey line marks the 95th-percentile level. Cluster bootstrapping of entire flights yielded 95 % confidence intervals of 3.2 to 15.6 kg h^{-1} for the transect-weighted estimator and 3.3 to 15.6 kg h^{-1} for the equal-flight-weighted estimator. The equal-flight-weighted estimate of approximately 11 kg h^{-1} is interpreted as the mean campaign-specific estimate, while the upper bootstrap confidence limit of approximately 16 kg h^{-1} provides a conservative quantification threshold.

S2.2.5 Comparison with Förster et al. (2025)

The empirical threshold derived here is consistent with the controlled-release experiment reported by Förster et al. (2025). In that experiment, two releases of approximately 21 kg h^{-1} were detected and quantified using the *HELiPOD* mass-balance approach, demonstrating its applicability to point-source emissions of approximately 20 kg h^{-1} under favourable conditions.

The two analyses provide complementary information. The controlled release represents a positive validation case in which a known emission produced a spatially coherent plume. In contrast, the present analysis statistically evaluates source-free measurements to determine the flux level at which an estimate becomes distinguishable from the variability, or noise, of the complete calculation method.

The controlled releases of approximately 21 kg h^{-1} lie above both the mean empirical estimate of approximately 11 kg h^{-1} and the conservative quantification threshold of approximately 16 kg h^{-1}. The successful detection and quantification of these releases therefore agree well with the independently derived null-flux threshold. Under particularly favourable conditions, characterized by steady winds, low background variability, and a well-mixed boundary layer, substantially smaller fluxes may be distinguishable from the methodological variability. Together, the positive validation experiment and the statistical null-flux analysis indicate that CH_4 emissions on the order of 20 kg h^{-1} can be quantified with the *HELiPOD* mass-balance method under suitable conditions, whereas fluxes near or below the conservative threshold should be interpreted more cautiously.

The derived threshold remains a coarse, campaign-specific estimate and may vary between campaigns and meteorological situations depending on background variability, wind conditions, boundary-layer structure, integration height, and sampling strategy. Nevertheless, the agreement with the controlled-release results suggests that the estimated order of magnitude is robust for the conditions represented by the present campaign.

S3 Supplement to Results

Table S5 summarises the meteorological conditions, plume characteristics, and flight-specific top-down CH_4 mass flux estimates derived from 32 MBEs conducted during 20 *HELiPOD* flights. Mean wind speeds ranged from 1.7 to 8.3 m s^{-1}, with an overall mean of 4.2 m s^{-1}. Wind-direction variability differed substantially among flights, with σDD values ranging from 8° to 73°. The largest variability generally occurred under weak-wind conditions, particularly during measurements in Region B, where complex topography and the developing boundary layer additionally affected the local wind field.

The estimated plume tops ranged from approximately 200 to 2200 m, reflecting differences in atmospheric stratification, source strength, and the downwind distance at which the plumes were probed. In general, measurements conducted farther from the source captured plumes at greater vertical extents, as the emitted air masses had more time to rise and disperse before reaching the measurement curtain. The highest plume tops were observed for B1, where measurements were conducted at distances of up to approximately 9 km from the facility cluster. By contrast, the lower plume tops observed for C1 and C2 should not be interpreted as a characteristic of sour production itself, as these plumes were generally probed at shorter distances of approximately 2 to 4 km from the targeted facilities.

Substantial regional differences are also evident in the derived mass fluxes. Estimates for the sweet facilities in Regions A and B ranged from approximately 60 to 2240 kg h^{-1}. Region B exhibited both the highest emission rates and the largest temporal variability, particularly for B1, where the measurements included a maintenance-related tank-venting event. Fluxes from B2 were lower but consistently ranged between approximately 250 and 560 kg h^{-1}. In Region A, A1 emitted between approximately 170 and 280 kg h^{-1}, while A2 remained comparatively stable between approximately 60 and 70 kg h^{-1}. By contrast, all estimates for the sour facilities C1 and C2 ranged between 1 and 15 kg h^{-1} and therefore did not exceed the conservative empirical quantification threshold of approximately 16 kg h^{-1}.

Figure S3 separates the regional cumulative distribution functions (CDFs) shown in Fig. 4b into individual assets, allowing differences within each region to be examined. At each enhancement threshold on the x-axis, the corresponding y-value represents the fraction of measurements exceeding that threshold. As the x-axis starts at a defined detection threshold of 3 ppb, the intersections of the curves with the y-axis indicate the fractions of measurements classified as detectable.

Table S5. Summary of top-down CH_4 mass flux estimates from MTG-Oman. Fluxes and associated uncertainties (1σ) are derived from the individual mass balance experiments (MBEs) conducted during the respective *HELiPOD* flights. FF and DD denote mean wind speed and wind direction, respectively, σDD the root-mean-square error of the wind direction, and Ø the average across all plume transects of the respective MBE. Bold values in the column "top of morning inversion/PBL" indicate cases in which the reported value corresponds to the planetary boundary layer (PBL) height. Of the 35 O&G MBEs conducted during the campaign, 32 were retained for quantification. Flight F21 is omitted because no measurement data were available; both MBEs of F04 were excluded because the upper part of the plume was not sufficiently sampled, and the second MBE of F03 was excluded because CH_4 enhancements were too small for reliable quantification. The rows "A1 Oil" and "A1 Gas" represent the source-specific decomposition of the retained F03 MBE and are not counted as additional MBEs. Regional "sum | mean" rows summarise the number of retained MBEs and the mean meteorological, plume, flux, and uncertainty parameters for Regions A, B, and C, respectively; the final row provides the corresponding overall values for all retained O&G MBEs. For the column "top of morning inversion/PBL", separate mean heights are reported for inversion layers and the PBL. Target-level mean fluxes and uncertainties are provided in Table 2 of the main document.

site	date	take-off local time	Flight	MBEs	MBE distance to source [m]	Ø FF [m s^{-1}]	Ø DD [°]	σ DD [°]	top of plume [m]	top of morning inversion/**PBL** [m]	flux [kg h^{-1}]	unc. [kg h^{-1}]
A1 O&G	14 Nov 23	10:39	F01	2	1500/2800	2.1	102	44	2200	**2200**	**280**	**180**
A1 O&G	16 Nov 23	08:42	F03	1	1500	6.8	121	10	475	800	**166**	**70**
A1 Oil	16 Nov 23	08:42	F03		1500	6.7	123	10	425	800	**80**	**30**
A1 Gas	16 Nov 23	08:42	F03		1500	6.7	123	10	443	800	**84**	**30**
A2	15 Nov 23	08:46	F02	2	1100/2100	5.9	113	8	574	**1900**	**61**	**60**
A2	17 Nov 23	08:58	F05	2	1500/2700	4.1	115	13	675	675	**72**	**80**
A2	18 Nov 23	08:56	F06	2	2200/3300	2.5	221	30	450	450	**65**	**40**
A, sum | mean				Σ9		4.3		21	875	642/**2050**	**115**	**82**
B1	21 Nov 23	14:21	F07	1	9200	3.5	108	22	2100	**2100**	**1870**	**540**
B1	24 Nov 23	08:28	F10	1	7400	2.4	3	37	900	900	**1240**	**480**
B1	24 Nov 23	14:21	F11	1	2500	1.7	245	73	1600	**1600**	**2240**	**320**
B1	26 Nov 23	15:02	F13	1	7800	4.6	144	16	2000	2000	**1800**	**320**
B2	23 Nov 23	10:20	F08	2	1400/2400	2.2	324	41	1300	1300	**254**	**170**
B2	23 Nov 23	14:42	F09	1	2600	2.5	291	38	1500	1500	**351**	**100**
B2	25 Nov 23	08:13	F12	3	1900/3000/4100	3.5	124	43	764	900	**563**	**80**
B, sum | mean				Σ10		2.9		39	1452	1320/**1850**	**1188**	**328**
C1	05 Dec 23	08:15	F18	1	1800	3.2	350	31	419	650	**1**	**10**
C1	05 Dec 23	14:53	F19	1	1700	7.8	34	11	357	2000	**1**	**1**
C1	09 Dec 23	07:58	F25	2	1800/1900	3.1	127	17	208	500	**3**	**10**
C2	06 Dec 23	08:12	F20	2	2500/3700	4.6	91	9	433	625	**5**	**30**
C2	07 Dec 23	14:28	F22	2	1700/3100	8.3	40	9	576	600	**4**	**30**
C2	08 Dec 23	07:57	F23	1	1700	2.6	39	41	350	600	**15**	**8**
C2	08 Dec 23	13:51	F24	2	1700/3100	5.4	26	11	527	**1450**	**4**	**30**
C2	09 Dec 23	13:51	F26	2	1800/3200	6.5	50	12	635	**1500**	**5**	**30**
C, sum | mean				Σ13		5.2		18	438	829/**1475**	**5**	**18**
A+B+C, sum | mean				Σ32		4.2		26	902	964/**1792**		

The asset-specific distributions reveal considerable variability within Regions A and C. Both assets in Region B show high detectable fractions of approximately 94 to 95 %, although Dataset 1 exhibits a higher fraction of intermediate enhancements than Dataset 2. Datasets 1 and 3 in Region A similarly show detectable enhancements for approximately 90 to 95 % of the measurements. In contrast, Dataset 2 in Region A has a lower detectable fraction of approximately 72 %, more closely resembling Datasets 1 and 2 in Region C, for which only 64 to 66 % of the measurements show detectable enhancements. Dataset 3 in Region C differs markedly from the other two assets in that region, exhibiting a similarly high detectable fraction and substantially larger enhancements that more closely resemble the higher-enhancement distributions in Regions A and B. Thus, the regional patterns shown in Fig. 4b reflect both broader regional differences and substantial asset-level variability.

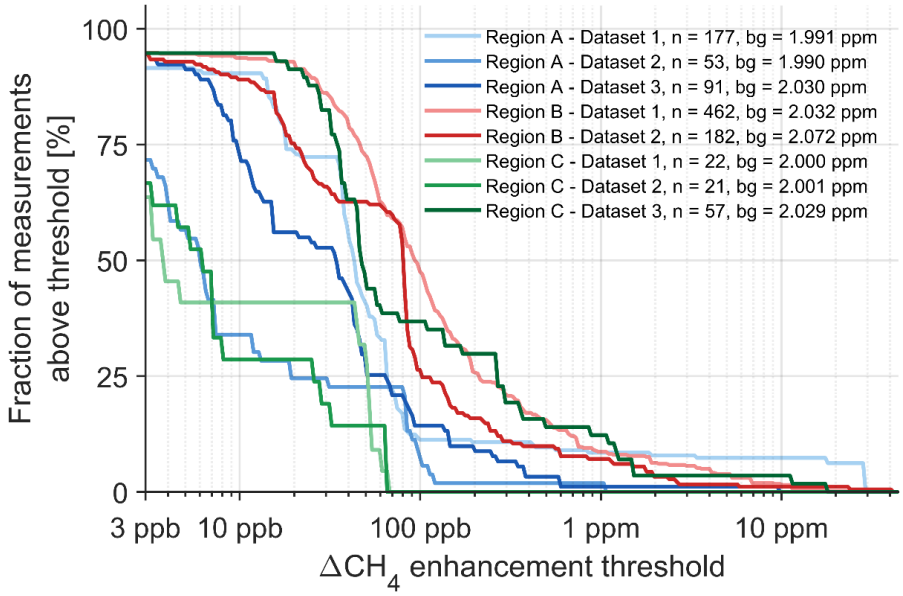


Figure S3. Cumulative distribution functions (CDFs) of CH_4 enhancements measured several metres downwind of *n* wells, shown separately for individual assets in Regions A, B, and C. For each asset, the atmospheric CH_4 background (bg) was defined as the 5th percentile of the respective dataset. Enhancements of at least 3 ppb above background were considered detectable. Compared with the regionally aggregated distributions in Fig. 4b, the asset-specific CDFs appear more step-like because they contain fewer data points, particularly for the assets in Region C.

An example of a measurement flight is shown in Fig. S4. Three consecutive mass balance experiments (MBEs) were performed downwind of an O&G facility at increasing distances of approximately 1.9, 3.0, and 4.1 km from the source. The first downwind MBE is shown in cross-sectional view in Fig. S4b, including the mobile ground-based transect at 0 m altitude used to constrain the lower part of the mass balance curtain. Repeated sampling of the same plume provides a consistency check for the mass balance approach, as comparable flux estimates from multiple downwind screens indicate that the emission remained sufficiently stable during the flight and that the plume was captured reliably. The individual MBE estimates were 580 ± 80 , 543 ± 77, and 567 ± 63 kg h^{-1} for the first, second, and third MBE, respectively. The mean wind speed was 3.5 m s^{-1}, with a mean wind direction of 124°. The plume remained confined below approximately 764 m, while a morning inversion was located at about 900 m. These conditions make Flight 12 a textbook example of airborne mass balance quantification, with the plume vertically constrained, repeatedly intercepted, and clearly separated from the surrounding background. The mean CH_4 emission rate derived from the three MBEs was 563 ± 80 kg h^{-1}, with observed CH_4 enhancements of up to 0.4 ppm.

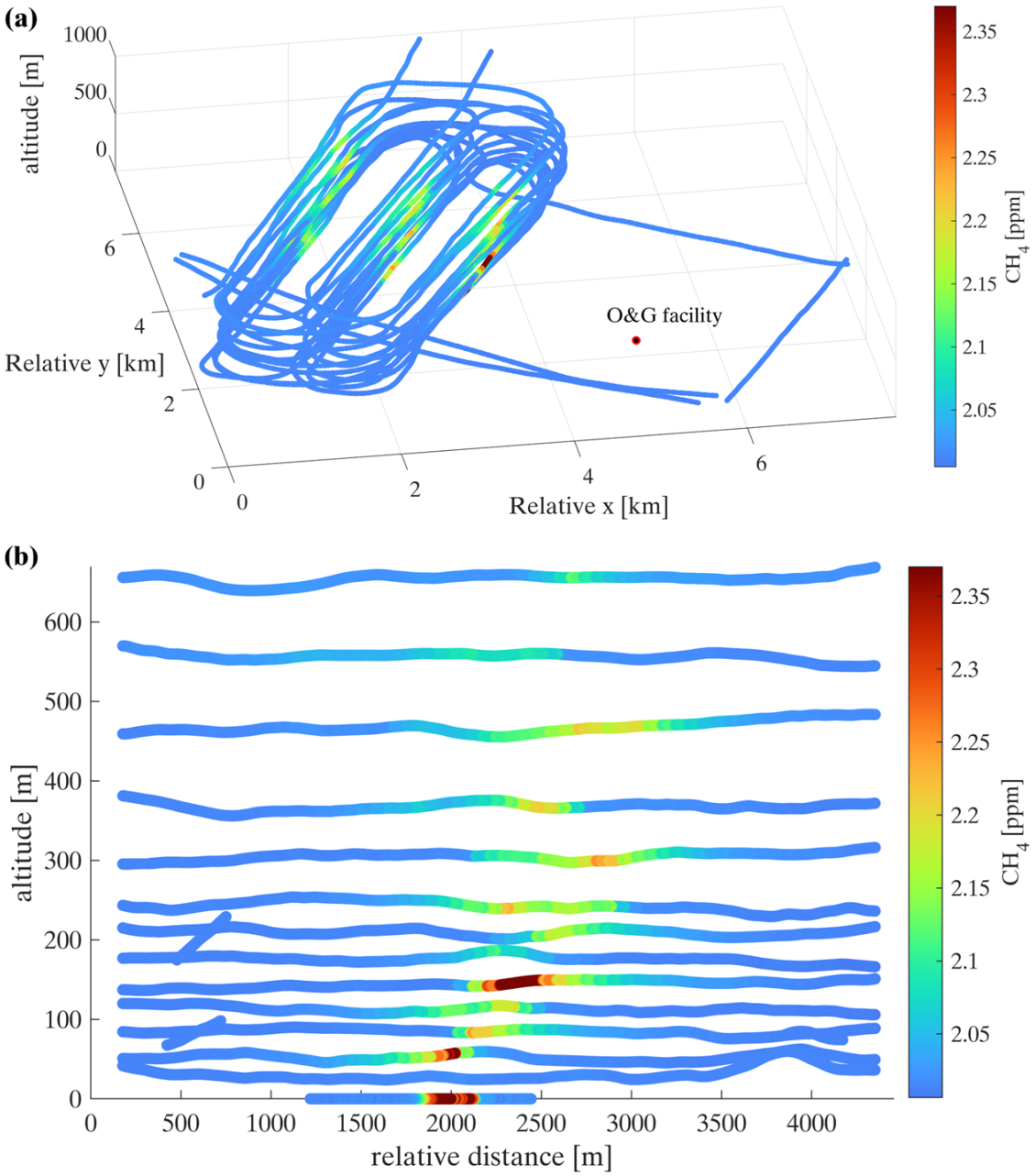


Figure S4. Three-dimensional view of Flight 12 conducted on 25 November 2023 in Region B. (a) The flight track is coloured according to the measured CH_4 concentration. Three consecutive downwind mass balance experiments (MBEs) were performed approximately 2, 3, and 4 km downwind of the O&G facility. Suitable mobile ground-based transects were available for all three MBEs and were incorporated into the respective mass balance calculations to constrain the lower part of the measurement curtains. (b) Cross-sectional view of the first downwind MBE, shown as an example, conducted at a distance of approximately 2 km from the facility. The corresponding mobile ground-based transect is shown at 0 m altitude. The CH_4 plume remained confined below approximately 760 m, while a morning inversion was located at about 900 m. The mean CH_4 emission rate derived from the three MBEs was 563 ± 80 kg h^{-1}.

Figure S5 shows Flight 24 as an example of the airborne measurements conducted in Region C. Two downwind MBEs were performed at an O&G facility, but CH_4 concentrations remained close to the regional background of approximately 2 ppm, and no coherent CH_4 plume was detected. The corresponding time series in Fig. S6 confirm the absence of distinct CH_4 enhancements in the measurements from both CH_4 instruments. In contrast, several distinct CO_2 enhancements were observed, most likely associated with encounters of flaring plumes, but these peaks were not accompanied by simultaneous CH_4 enhancements. This indicates combustion-related CO_2 emissions without corresponding detectable emissions of uncombusted

CH_4 during the plume passages. Consistent with this non-detection, the corresponding CH_4 flux estimates remained below the empirical *HELiPOD* quantification threshold of approximately 16 kg h^{-1}. Together, Figs. S5 and S6 illustrate a representative non-detection case for the investigated facilities in Region C.

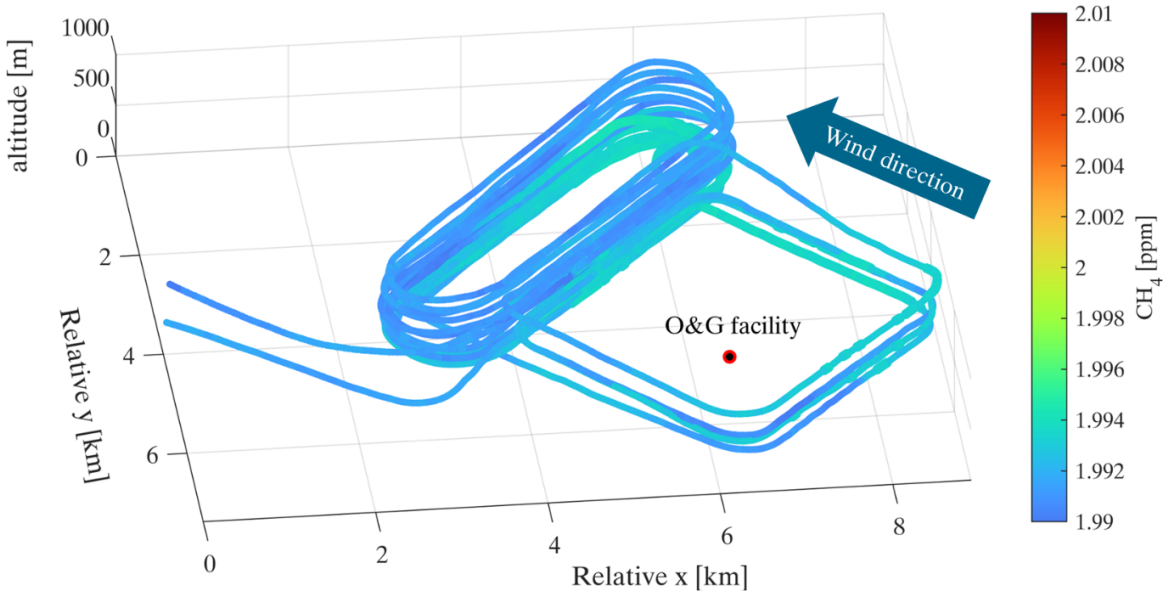


Figure S5. Three-dimensional view of Flight 24 conducted on 8 December 2023 in Region C. The flight track is coloured according to the measured CH_4 concentration. Two downwind mass balance experiments (MBEs) were conducted at an O&G facility, but CH_4 concentrations remained close to the regional background of approximately 2 ppm, and no coherent CH_4 plume was detected. The flight is representative of the airborne measurements at the investigated facilities in Region C, where no detectable CH_4 emissions were observed. Corresponding CH_4 and CO_2 time series are shown in Fig. S6.

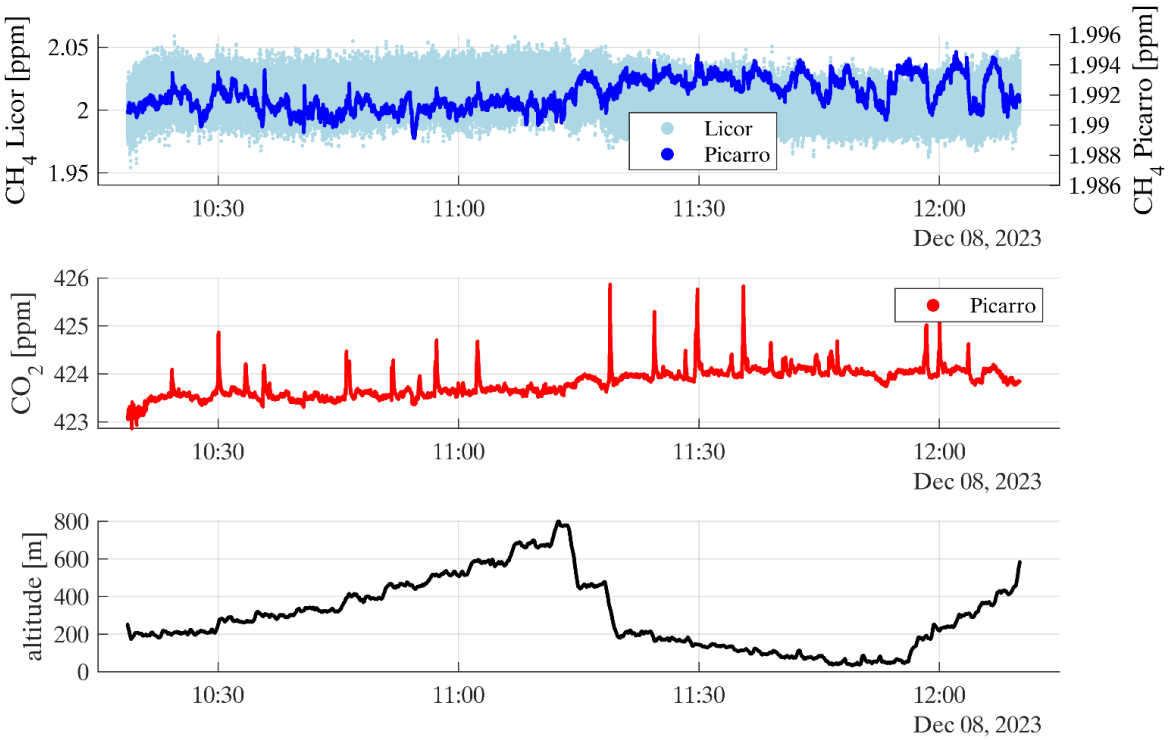


Figure S6. Time series of CH_4 mole fractions measured by the LI-COR and Picarro instruments, CO_2 mole fractions measured by the Picarro instrument, and flight altitude during Flight 24 on 8 December 2023 in Region C. Both CH_4 measurements remained close to the regional background of approximately 2 ppm, and no distinct CH_4 enhancements were detected during the downwind MBEs. In contrast, distinct CO_2 enhancements were observed during plume passages, indicating flaring-related combustion signals without corresponding detectable CH_4 emissions.

S4 Loss rate calculation and conversion

A CH_4 loss rate relates annual CH_4 emissions to a corresponding annual hydrocarbon-production quantity and expresses the ratio as a percentage. Normalisation facilitates comparisons among assets, regions, inventories, and studies with different absolute production volumes, but the resulting value depends on the denominator. A gas-production-normalised loss rate relates CH_4 emissions to the mass of CH_4 contained in marketed gas and approximates the fraction of produced CH_4 emitted to the atmosphere. An O&G-production-normalised loss rate instead relates CH_4 emissions to combined marketed oil and gas production and provides a broader production-based metric for assets and regions producing different hydrocarbon mixtures. Hydrocarbon production is reported in different units across data sources and studies: gas production is commonly expressed as a volume, oil production as a volume or mass, and combined O&G production on an energy-equivalent basis using barrels of oil equivalent (BOE). Other studies report CH_4 intensities directly in units such as kg CH_4 BOE^{-1} or g CH_4 MJ^{-1}. In this study, combined marketed O&G production is primarily taken from data reported in MBOE yr^{-1}, where MBOE denotes million barrels of oil equivalent, and subsequently converted to a common oil-equivalent mass basis.

The two denominators require different conversions. For gas-normalised loss rates, gas production reported directly as a volume was converted to CH_4 mass using the CH_4 volume fraction and CH_4 density at standard reference conditions. Where only MBOE data were available, gas production was first converted to volume using 6000 ft^3 BOE^{-1}. This follows the volume-based approach applied by Schneising et al. (2020). The CH_4 volume fraction of 0.92 assumed by Chen et al. (2023) was retained only when converting their reported gas-production-normalised loss rate to the O&G-production-normalised basis in Sect. S4.5. For gas-normalised values calculated for this study, the Oman inventories, and the estimate from Gasim et al. (2024), a CH_4 volume fraction of 1.00 was applied. This CH_4-equivalent convention was used for the gas-production-normalised values compared with the 0.2 % Oil and Gas Climate Initiative (OGCI, 2025) target in Fig. S7. Because that target is defined relative to marketed gas production, it is not shown in the O&G-production-normalised comparison in Fig. 7, which uses a different denominator. For O&G-normalised loss rates, total marketed O&G production was already reported as combined MBOE, meaning that the gas contribution had already been expressed in BOE. The complete O&G production quantity was therefore converted uniformly to an oil-equivalent mass using 136.4 kg BOE^{-1} (BP, 2021). This produces a BOE-based CH_4-intensity metric comparable to values reported in kg CH_4 BOE^{-1}, such as those of Gasim et al. (2024), and avoids applying a separate gas-mass conversion within the combined O&G denominator.

Subsections S4.1 and S4.2 define the two loss rates. Subsection S4.3 describes the conversion of gas production from either reported volume or MBOE yr^{-1} to the CH_4-mass denominator, while Subsection S4.4 describes the conversion of total O&G production from MBOE yr^{-1} to the oil-equivalent mass denominator. Subsection S4.5 gives the conversion between gas- and O&G-production-normalised loss rates, Subsection S4.6 documents the literature-specific conversions, Subsection S4.7 summarises the approach, and Subsection S4.8 provides all constants, auxiliary inputs, original literature values, and derived results required to reproduce the calculations.

S4.1 Gas-production-normalised loss rate

The gas-production-normalised loss rate was calculated as

$$\boldsymbol{LR_{gas} = 100\ \frac{E_{CH_4}}{P_{CH_4,gas}}}, \tag{S2}$$

where LR_{gas} is the gas-production-normalised CH_4 loss rate in %, E_{CH_4} is the annual CH_4 emission in kt CH_4 yr^{-1}, and $P_{CH_4,gas}$ is the annual CH_4 mass contained in marketed gas in kt CH_4 yr^{-1}. Equation S2 was used for all gas-normalised values calculated in this study. Literature values already reported as gas-production-normalised loss rates were used directly.

S4.2 O&G-production-normalised loss rate

The O&G-production-normalised loss rate on the oil-equivalent mass basis used in this study was calculated as

$$\boldsymbol{LR_{O\&G} = 100\,\frac{E_{CH_4}}{P_{O\&G,oil-eq}}},\tag{S3}$$

where $LR_{O\&G}$ is the O&G-production-normalised CH_4 loss rate in %, and $P_{O\&G,oil-eq}$ is total annual marketed O&G production expressed as an oil-equivalent mass in kt yr^{-1}. This is the primary metric used in the main text because half of the investigated assets produced oil only.

S4.3 Conversion of gas production from MBOE yr^{-1} to kt CH_4 yr^{-1}

Following Schneising et al. (2020), one BOE of natural gas was represented by 6000 ft^3. Using 1 ft^3 = 0.02831 m^3 gives

$$\boldsymbol{V_{gas/BOE} = 6000 * 0.02831 = 169.9\ m^3\ BOE^{-1}}.\tag{S4}$$

The CH_4 density at the standard reference conditions used by Schneising et al. (2020), $T = 288.15$ K and $p = 101325$ Pa, was calculated with the ideal-gas law:

$$\boldsymbol{\rho_{CH_4} = \frac{pM_{CH_4}}{RT} = 0.6784\ kg\ m^{-3}},\tag{S5}$$

where $M_{CH_4} = 0.01604$ kg mol^{-1} is the molar mass of CH_4, and $R = 8.3145$ J mol^{-1} K^{-1} is the universal gas constant. For the gas-normalised values calculated here, a CH_4 volume fraction $x_{CH_4} = 1.00$ was applied. Chen et al. (2023) instead assumed a CH_4 volume fraction of 0.92 for Oman, as retained in Sect. S4.5. The CH_4 mass corresponding to one gas BOE is

$$\boldsymbol{m_{CH_4/BOE} = V_{gas/BOE}\,x_{CH_4}\,\rho_{CH_4} = 115.3\ kg\ CH_4\ BOE^{-1}}.\tag{S6}$$

Annual gas production was therefore converted as

$$\boldsymbol{P_{CH_4,gas}\left[kt\ yr^{-1}\right] = P_{gas}\left[MBOE\ yr^{-1}\right] * 115.3\left[kg\ CH_4\ BOE^{-1}\right]}.\tag{S7}$$

The factors of 10^6 for MBOE to BOE and kg to kt cancel in Equation S7. Thus, the numerical conversion factor in kg CH_4 BOE^{-1} can be multiplied directly by production in MBOE yr^{-1} to obtain kt CH_4 yr^{-1}. Where gas production was available directly as a volume, as for the data of the Omani Ministry of Energy and Mining (MEM, 2020, 2023), the reported volume was converted directly to CH_4 mass using the CH_4 volume fraction of 1.00 and the density defined above, without the intermediate BOE conversion.

S4.4 Conversion of total O&G production from MBOE yr^{-1} to the oil-equivalent mass basis

Total marketed O&G production reported in MBOE yr^{-1} was converted to an oil-equivalent mass using $m_{oil,eq/BOE} = 136.4$ kg BOE^{-1} (BP, 2021):

$$\boldsymbol{P_{O\&G,oil-eq}\left[kt\ yr^{-1}\right] = P_{O\&G}\left[MBOE\ yr^{-1}\right] * 136.4\left[kg\ BOE^{-1}\right]}.\tag{S8}$$

As in Equation S7, the factors of 10^6 cancel. Because the reported O&G production is already the combined oil and gas quantity in BOE, Equation S8 is applied to the full total. The gas share is not converted separately within this denominator.

S4.5 Conversion of gas-production-normalised to O&G-production-normalised loss rates

When a study reported a gas-production-normalised loss rate and the corresponding oil and gas production data were available, the O&G-production-normalised loss rate was obtained by rescaling the denominator:

$$\boldsymbol{LR_{\mathrm{O\&G}} = LR_{\mathrm{gas}} \frac{P_{\mathrm{CH_4,gas}}}{P_{\mathrm{O\&G,oil-eq}}} = LR_{\mathrm{gas}} \frac{P_{\mathrm{gas}}\, m_{\mathrm{CH_4/BOE}}}{\left(P_{\mathrm{oil}} + P_{\mathrm{gas}}\right) m_{\mathrm{oil,eq/BOE}}}.} \quad \text{(S9)}$$

Here, P_{oil} and P_{gas} are expressed in the same unit, MBOE yr^{-1}. Equation S9 was applied to the Oman loss rate reported by Chen et al. (2023). Using $P_{\mathrm{oil}} = 359$ MBOE yr^{-1}, $P_{\mathrm{gas}} = 224$ MBOE yr^{-1}, $x_{\mathrm{CH_4}} = 0.92$, $m_{\mathrm{CH_4/BOE}} = 106.1$ kg CH$_4$ BOE^{-1}, and $m_{\mathrm{oil,eq/BOE}} = 136.4$ kg BOE^{-1} gives a conversion factor of 0.3. The reported gas-normalised estimate of 8.9 %, with a range of 4.5 to 13.4 %, therefore corresponds to an O&G-normalised estimate of 2.7 %, with a range of 1.4 to 4.0 %, on the oil-equivalent mass basis used here.

S4.6 Literature-specific conversions to the oil-equivalent mass basis

S4.6.1 Schneising et al. (2020)

Schneising et al. (2020) calculate energy-based O&G leakage rates by expressing both CH$_4$ emissions and combined O&G production in BOE. Natural-gas production is converted to BOE using 6000 ft^3 BOE^{-1}, whereas emitted CH$_4$ mass is converted to natural-gas-equivalent BOE at 288.15 K and 101325 Pa using a CH$_4$ volume fraction of 0.93. Following the procedure in Eqs. S4 to S6, the CH$_4$ mass corresponding to one natural-gas-equivalent BOE is

$$\boldsymbol{m_{\mathrm{CH_4/BOE,Sch}} = 169.9 \times 0.93 \times 0.6784 = 107.2\ \mathrm{kg\ CH_4\ BOE^{-1}}.} \quad \text{(S10)}$$

Thus, although the combined O&G production used by Schneising et al. (2020) is already expressed in BOE and requires no further conversion, their reported percentage is based on natural-gas-equivalent BOE in the emission numerator. In contrast, the mass-based metric used in this study retains emissions as CH$_4$ mass and assigns an oil-equivalent mass of 136.4 kg to each BOE of combined O&G production. Their reported rates were therefore rescaled once to the oil-equivalent mass basis as

$$\boldsymbol{LR_{\mathrm{O\&G}} = LR_{\mathrm{Sch}} \frac{m_{\mathrm{CH_4/BOE,Sch}}}{m_{\mathrm{oil,eq/BOE}}} = LR_{\mathrm{Sch}} \frac{107.2}{136.4} = LR_{\mathrm{Sch}} * 0.786.} \quad \text{(S11)}$$

This conversion changes only the normalisation basis of the reported percentage; it does not reconvert the underlying O&G production data.

S4.6.2 Conrad et al. (2023)

Conrad et al. (2023) report CH$_4$ intensity, $I_{\mathrm{g/MJ}}$, in g CH$_4$ MJ^{-1}. Multiplication by the energy content of one BOE converts this intensity to CH$_4$ mass per BOE, with 6.119 GJ BOE^{-1} corresponding to 6119 MJ BOE^{-1}. The factor of 1000 then converts grams of CH$_4$ to kilograms, while the factor of 100 converts the resulting dimensionless mass ratio to percent. Using an oil-equivalent mass of 136.4 kg BOE^{-1}, the reported values were therefore converted directly as

$$\boldsymbol{LR_{\mathrm{O\&G}} = I_{\mathrm{g/MJ}} \frac{6119\ \mathrm{MJ\ BOE^{-1}}}{1000\ \mathrm{g\ kg^{-1}}} \frac{100}{136.4\ \mathrm{kg\ BOE^{-1}}} = I_{\mathrm{g/MJ}} * 4.49.} \quad \text{(S12)}$$

S4.6.3 Gasim et al. (2024)

Gasim et al. (2024) report O&G CH$_4$ intensity, $I_{\mathrm{kg/BOE}}$, in kg CH$_4$ BOE^{-1}. The corresponding percentage on the oil-equivalent mass basis was calculated as

$$LR_{O\&G} = I_{kg/BOE}\frac{100}{136.4} = I_{kg/BOE} * 0.73. \quad \text{(S13)}$$

The central value and the lower and upper bounds were converted with the same factor. The bounds were approximated visually from the error bar reported by Gasim et al. (2024).

S4.7 Summary of the normalisation approach used in this study

In summary, gas-production-normalised loss rates calculated in this study use the actual CH_4 mass in marketed gas obtained from gas volume, CH_4 fraction, and CH_4 density (Eqs. S2 and S4 to S7). Reported gas volumes were used directly, while production available only in MBOE was first converted to volume. O&G-production-normalised loss rates use total marketed O&G production on a uniform oil-equivalent mass basis (Eqs. S3 and S8). Equation S9 converts a gas-normalised value to the O&G basis only when the matching oil and gas production inputs are available. The literature-specific conversions in Eqs. S10 to S13 are each applied once to the originally reported metric. Literature values already reported as gas-production-normalised loss rates remain unchanged.

S4.8 Loss rate data

Table S6. Constants, assumptions, auxiliary inputs, and derived conversion factors used in the loss-rate calculations.

Parameter	Value	Unit	Definition or source
Oil-equivalent mass per BOE	136.4	kg BOE^{-1}	BP (2021)
Natural-gas volume per BOE	6000	ft^3 BOE^{-1}	Schneising et al. (2020); EIA conversion basis
Cubic-foot to cubic-metre conversion	0.02831	m^3 ft^{-3}	Unit conversion
Natural-gas volume per BOE	169.9	m^3 BOE^{-1}	Eq. S4
Gas-volume-to-BOE factor	5.883	BOE per 1000 m^3	BP (2021)
CH_4 volume fraction used by Chen et al. (2023)	0.92	fraction	Chen et al. (2023)
CH_4 volume fraction used by Schneising et al. (2020)	0.93	fraction	Schneising et al. (2020)
Reference temperature	288.15	K	Schneising et al. (2020)
Reference pressure	101325	Pa	Schneising et al. (2020)
Universal gas constant	8.3145	J mol^{-1} K^{-1}	Mohr et al. (2025; 2022 CODATA adjustment)
CH_4 molar mass	0.01604	kg mol^{-1}	NIST Chemistry WebBook (Linstrom, 1997)
CH_4 density at reference conditions	0.6784	kg m^{-3}	Eq. S5
CH_4 mass per gas BOE, xCH_4 = 0.92	106.1	kg CH_4 BOE^{-1}	Eq. S9/ Chen conversion
CH_4 mass per gas BOE, xCH_4 = 0.93	107.2	kg CH_4 BOE^{-1}	Eq. S10
CH_4 mass per gas BOE, xCH_4 = 1.00	115.3	kg CH_4 BOE^{-1}	Eq. S6
Annualisation factor	8.76	kt yr^{-1} per t h^{-1}	Unit conversion
BOE energy conversion	6.119	GJ BOE^{-1}	BP (2021)
Schneising-to-oil-equivalent factor	0.786	dimensionless	Eq. S11
Conrad g CH_4 MJ^{-1} conversion factor	4.49	% per (g CH_4 MJ^{-1})	Eq. S12
Gasim kg CH_4 BOE^{-1} conversion factor	0.73	% per (kg CH_4 BOE^{-1})	Eq. S13
Chen 2019 oil production	359	MBOE yr^{-1}	EIA, input for Eq. S9
Chen 2019 gas production	224	MBOE yr^{-1}	EIA, input for Eq. S9
Chen gas-to-O&G conversion factor	0.3	dimensionless	Eq. S9

Table S7. Input data and derived CH_4 loss rates for the measurement-based emission estimates obtained for the investigated Omani assets in 2023. Total O&G production was converted from MBOE yr^{-1} to the oil-equivalent mass basis using Eq. S8, while gas production was converted from MBOE yr^{-1} to CH_4 mass using Eqs. S4 to S7. Gas-production-normalised CH_4 loss rates were calculated using Eq. S2, and O&G-production-normalised CH_4 loss rates using Eq. S3. Two production scenarios were considered based on estimates from Rystad Energy and Wood Mackenzie. The lower- and upper-bound cases combine the lower emission estimate with the higher production estimate and the upper emission estimate with the lower production estimate, respectively. Central loss-rate estimates correspond to the midpoint between these bounds, and the reported uncertainties represent half of their difference.

Including the super-emitting event (approximately 1 t h^{-1})

	Total O&G production		Gas production		CH_4 emissions		CH_4 loss rate		
Scenario	[MBOE yr^{-1}]	[kt yr^{-1}]	[MBOE yr^{-1}]	[kt CH_4-eq. yr^{-1}]	[t h^{-1}]	[kt yr^{-1}]	O&G [%]	Gas [%]	Remarks
Rystad	76	10408	29	3351	2.5	21.67	0.21	0.65	production scenario
Wood Mackenzie	85	11558	40	4667	2.5	21.67	0.19	0.46	production scenario
Lower bound	85	11558	40	4667	1.7	15.00	0.13	0.32	lower emissions + higher production
Upper bound	76	10408	29	3351	3.2	28.35	0.27	0.85	higher emissions + lower production
Central estimate							**0.20**	**0.58**	
Uncertainty							**0.07**	**0.26**	

Excluding the super-emitting event (approximately 1 t h^{-1})

Rystad	76	10408	29	3351	1.5	12.91	0.12	0.39	production scenario
Wood Mackenzie	85	11558	40	4667	1.5	12.91	0.11	0.28	production scenario
Lower bound	85	11558	40	4667	0.7	6.24	0.05	0.13	lower emissions + higher production
Upper bound	76	10408	29	3351	2.2	19.59	0.19	0.58	higher emissions + lower production
Central estimate							**0.12**	**0.36**	
Uncertainty							**0.07**	**0.23**	

Table S8. Input data and derived CH_4 loss rates for inventory-based estimates for Oman. Production data were matched to the respective inventory years. Total O&G production was converted to the oil-equivalent mass basis using Eq. S8. Gas production reported by Omani Ministry of Energy and Mining (MEM, 2020, 2023) as volume was converted directly to CH_4 mass using the CH_4 fraction and density defined in Sect. S4.3. Gas-production-normalised CH_4 loss rates were calculated using Eq. S2, and O&G-production-normalised CH_4 loss rates using Eq. S3. M denotes million.

		O&G production		Gas production		CH_4 emissions		CH_4 loss rate	
Inventory	Reference year	[MBOE yr^{-1}]	[kt oil-eq. yr^{-1}]	[M m^3 d^{-1}]	[kt CH_4-eq. yr^{-1}]	[t h^{-1}]	[kt yr^{-1}]	O&G [%]	Gas [%]
GFEI	2020	610	83200	122.0	30213	27.1	237	0.28	0.78
IEA	2023	689	93978	142.5	35289	77.1	675	0.72	1.91
EDGAR	2023	689	93978	142.5	35289	99.8	874	0.93	2.48
CAMS	2023	689	93978	142.5	35289	123.6	1083	1.15	3.07
CEDS	2023	689	93978	142.5	35289	264.6	2318	2.47	6.57

Table S9. Literature values used for the comparison of O&G-production-normalised CH_4 loss rates. Schneising et al. (2020) values were converted using Eqs. S10 and S11, Conrad et al. (2023) values using Eq. S12, the Chen et al. (2023) value using Eq. S9, and the Gasim et al. (2024) value using Eq. S13. The table provides the original reported values and the corresponding values on the common oil-equivalent mass basis. Rows are ordered by increasing calculated central O&G-production-normalised loss rate. The constants and auxiliary inputs required for all conversions are listed in Table S6.

				Reported			Calculated O&G loss rate [%]		
Study	Region	Reference year(s)	Reported metric	lower	value	upper	lower	value	upper
Conrad et al. (2023)	British Columbia	2021	Methane intensity [g CH_4 MJ^{-1}]	0.057	0.065	0.075	0.26	0.29	0.34
Gasim et al. (2024)	Oman	2023	Methane intensity [kg CH_4 BOE^{-1}]	0.30	0.65	1.00	0.22	0.48	0.73
Schneising et al. (2020)	Appalachia	2018–2019	Energy-based O&G loss rate [%]	0.8	1.2	1.6	0.63	0.94	1.26
Conrad et al. (2023)	Western Canada	2018–2020	Methane intensity [g CH_4 MJ^{-1}]	0.168	0.222	0.285	0.75	1.00	1.28
Schneising et al. (2020)	Bakken	2018–2019	Energy-based O&G loss rate [%]	0.5	1.3	2.1	0.39	1.02	1.65
Schneising et al. (2020)	Permian	2018–2019	Energy-based O&G loss rate [%]	0.8	1.3	1.8	0.63	1.02	1.41
Schneising et al. (2020)	Eagle Ford	2018–2019	Energy-based O&G loss rate [%]	0.7	1.4	2.1	0.55	1.10	1.65
Conrad et al. (2023)	United States	2015	Methane intensity [g CH_4 MJ^{-1}]	0.220	0.252	0.293	0.99	1.13	1.31
Conrad et al. (2023)	Alberta	2021	Methane intensity [g CH_4 MJ^{-1}]	0.221	0.257	0.317	0.99	1.15	1.42
Chen et al. (2023)	Oman	2019	Gas-normalised loss rate [%]	4.5	8.9	13.4	1.35	2.67	4.02
Schneising et al. (2020)	Anadarko	2018–2019	Energy-based O&G loss rate [%]	2.8	3.9	5.0	2.20	3.07	3.93
Schneising et al. (2020)	Turkmenistan	2018–2019	Energy-based O&G loss rate [%]	2.6	4.1	5.6	2.04	3.22	4.40

Table S10. Literature values used for the comparison of gas-production-normalised CH_4 loss rates. Reported gas-normalised values were used directly. For Gasim et al. (2024), the gas-normalised loss rate was calculated using Eq. S2 from the reported CH_4 emissions and gas production directly as volume (in million m^3 d^{-1}) as reported by the Omani Ministry of Energy and Mining (MEM, 2020, 2023); the emission bounds were approximated visually from the published error bar.

				Gas-normalised CH_4 loss rate [%]		
Study	Region	Reference year(s)	Reported metric	lower	value	upper
Gasim et al. (2024)	Oman	2023	CH_4 emissions [kt yr^{-1}] and gas production [M m^3 d^{-1}]	0.57	1.33	1.98
Zavala-Araiza et al. (2015)	Barnett Shale, United States	2013	Gas-normalised loss rate [%]	1.2	1.5	1.9
Shen et al. (2022)	Canada	2018–2020	Gas-normalised loss rate [%]		1.8	
Shen et al. (2022)	United States	2018–2020	Gas-normalised loss rate [%]		2.0	
Alvarez et al. (2018)	United States	2015	Gas-normalised loss rate [%]	2.0	2.3	2.7
Riddick et al. (2024)	Delaware Basin, United States	2020	Gas-normalised loss rate [%]		2.8	
Shen et al. (2022)	Permian Basin, United States	2018–2020	Gas-normalised loss rate [%]	3.5	4.1	4.6
Chen et al. (2023)	Oman	2019	Gas-normalised loss rate [%]	4.5	8.9	13.4

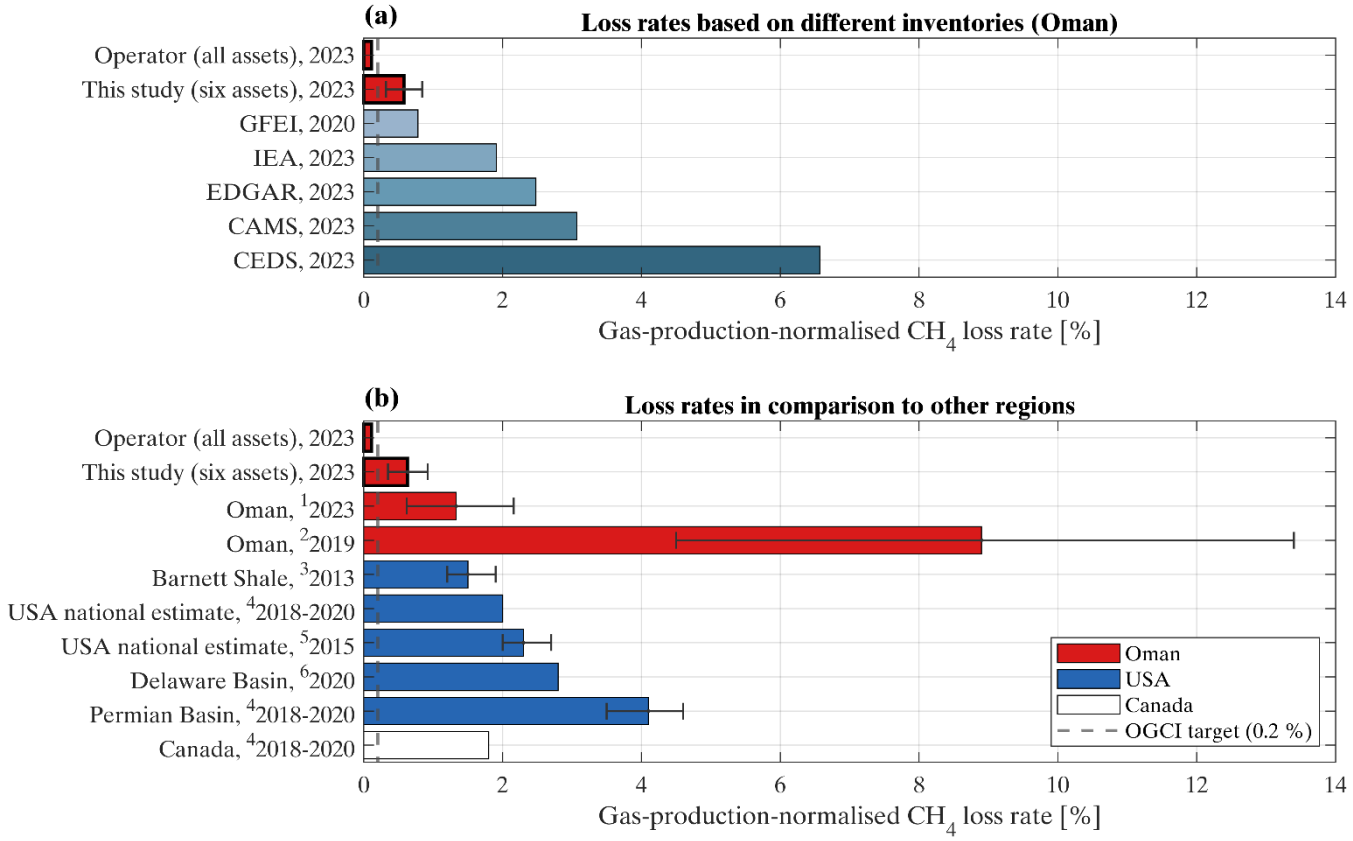


Figure S7. Gas-production-normalised CH_4 loss rates from this study compared with (a) the operator-reported estimate and estimates derived from different emission inventories for Oman and (b) estimates reported for other onshore O&G-producing regions in Oman, the United States, and Canada. Inventory-based loss rates in panel (a) were calculated from the respective emission estimates and year-matched gas production statistics from MEM (Table S8). Loss rates in panel (b) were taken directly from the respective studies where available. For Gasim et al. (2024), the gas-normalised loss rate was calculated from the reported CH_4 emissions and MEM (2020, 2023) gas production, while the uncertainty range was approximated visually from the published error bars. The error bar for this study accounts for uncertainties in the measured emissions and differences between the production estimates from Rystad Energy and Wood Mackenzie (Sect. 2.5). The dashed line indicates the OGCI target of 0.2 %. The input data and calculations for this study and the publicly available comparison estimates are provided in Tables S7, S8, and S10. [1]Gasim et al., 2024, [2]Chen et al., 2023, [3]Zavala-Araiza et al., 2015, [4]Shen et al., 2022, [5]Alvarez et al., 2018, [6]Riddick et al., 2024

References

Alvarez, R. A., Zavala-Araiza, D., Lyon, D. R., Allen, D. T., Barkley, Z. R., Brandt, A. R., Davis, K. J., Herndon, S. C., Jacob, D. J., Karion, A., Kort, E. A., Lamb, B. K., Lauvaux, T., Maasakkers, J. D., Marchese, A. J., Omara, M., Pacala, S. W., Peischl, J., Robinson, A. L., Shepson, P. B., Sweeney, C., Townsend-Small, A., Wofsy, S. C., and Hamburg, S. P.: Assessment of methane emissions from the U.S. oil and gas supply chain, Science, 361, 186–188, https://doi.org/10.1126/science.aar7204, 2018.

BP: Approximate conversion factors, https://www.bp.com/content/dam/bp/business-sites/en/global/corporate/pdfs/energy-economics/statistical-review/bp-stats-review-2022-approximate-conversion-factors.pdf, last access: 21 August 2026, 2021.

Chen, Z., Jacob, D. J., Gautam, R., Omara, M., Stavins, R. N., Stowe, R. C., Nesser, H., Sulprizio, M. P., Lorente, A., Varon, D. J., Lu, X., Shen, L., Qu, Z., Pendergrass, D. C., and Hancock, S.: Satellite quantification of methane emissions and oil–gas methane intensities from individual countries in the Middle East and North Africa: implications for climate action, Atmospheric Chemistry and Physics, 23, 5945–5967, https://doi.org/10.5194/acp-23-5945-2023, 2023.

Conrad, B. M., Tyner, D. R., Li, H. Z., Xie, D., and Johnson, M. R.: A measurement-based upstream oil and gas methane inventory for Alberta, Canada reveals higher emissions and different sources than official estimates, Commun Earth Environ, 4, 416, https://doi.org/10.1038/s43247-023-01081-0, 2023.

Crippa, M., Guizzardi, D., Muntean, M., Schaaf, E., Dentener, F., van Aardenne, J. A., Monni, S., Doering, U., Olivier, J. G. J., Pagliari, V., and Janssens-Maenhout, G.: Gridded emissions of air pollutants for the period 1970–2012 within EDGAR v4.3.2, Earth System Science Data, 10, 1987–2013, https://doi.org/10.5194/essd-10-1987-2018, 2018.

Currie, L. A.: Limits for qualitative detection and quantitative determination. Application to radiochemistry, Anal. Chem., 40, 586–593, https://doi.org/10.1021/ac60259a007, 1968.

Currie, L. A.: Detection and quantification limits: origins and historical overview, Analytica Chimica Acta, 391, 127–134, https://doi.org/10.1016/S0003-2670(99)00105-1, 1999.

Förster, E., Huntrieser, H., Lichtenstern, M., Pätzold, F., Bretschneider, L., Schlerf, A., Bollmann, S., Lampert, A., Nęcki, J., Jagoda, P., Swolkień, J., Pasternak, D., Field, R. A., and Roiger, A.: A helicopter-based mass balance approach for quantifying methane emissions from industrial activities, applied for coal mine ventilation shafts in Poland, Atmos. Meas. Tech., 18, 7153–7176, https://doi.org/10.5194/amt-18-7153-2025, 2025.

Gasim, A., Matar, W., Muhsen, A., Anand, S., and Guery, J.: Using Satellite Technology to Measure Methane Emissions in Arabian Gulf Countries, King Abdullah Petroleum Studies and Research Center, https://doi.org/10.30573/KS--2024-DP38, 2024.

Hyslop, N. P. and White, W. H.: An Empirical Approach to Estimating Detection Limits Using Collocated Data, Environ. Sci. Technol., 42, 5235–5240, https://doi.org/10.1021/es7025196, 2008.

Linstrom, P.: NIST Chemistry WebBook, NIST Standard Reference Database 69, https://doi.org/10.18434/T4D303, 1997.

McDuffie, E. E., Smith, S. J., O'Rourke, P., Tibrewal, K., Venkataraman, C., Marais, E. A., Zheng, B., Crippa, M., Brauer, M., and Martin, R. V.: A global anthropogenic emission inventory of atmospheric pollutants from sector- and fuel-specific sources (1970–2017): an application of the Community Emissions Data System (CEDS), Earth Syst. Sci. Data, 12, 3413–3442, https://doi.org/10.5194/essd-12-3413-2020, 2020.

MEM: Ministry of Energy and Minerals of Oman (MEM) Annual Report 2020, https://www.scribd.com/document/750886833/MEM-Annual-Report-2020-English-small-compressed (last access: 21 August 2026), 2020.

MEM: Ministry of Energy and Minerals of Oman (MEM) Annual Report 2023, https://www.scribd.com/document/823696186/MEM-Annual-Report-2023 (last access: 29 September 2025), 2023.

Mohr, P. J., Newell, D. B., Taylor, B. N., and Tiesinga, E.: CODATA recommended values of the fundamental physical constants: 2022, Rev. Mod. Phys., 97, 025002, https://doi.org/10.1103/RevModPhys.97.025002, 2025.

OGCI: OGCI Progress Report 2025, https://www.ogci.com/wp-content/uploads/2025/10/251017_OGCI_ProgressReport2025_V21.2.pdf, 2025.

Riddick, S. N., Mbua, M., Santos, A., Hartzell, W., and Zimmerle, D. J.: Potential Underestimate in Reported Bottom-up Methane Emissions from Oil and Gas Operations in the Delaware Basin, Atmosphere, 15, 202, https://doi.org/10.3390/atmos15020202, 2024.

Scarpelli, T. R., Jacob, D. J., Grossman, S., Lu, X., Qu, Z., Sulprizio, M. P., Zhang, Y., Reuland, F., Gordon, D., and Worden, J. R.: Updated Global Fuel Exploitation Inventory (GFEI) for methane emissions from the oil, gas, and coal sectors: evaluation with inversions of atmospheric methane observations, Atmospheric Chemistry and Physics, 22, 3235–3249, https://doi.org/10.5194/acp-22-3235-2022, 2022.

Schneising, O., Buchwitz, M., Reuter, M., Vanselow, S., Bovensmann, H., and Burrows, J. P.: Remote sensing of methane leakage from natural gas and petroleum systems revisited, Atmospheric Chemistry and Physics, 20, 9169–9182, https://doi.org/10.5194/acp-20-9169-2020, 2020.

Shen, L., Gautam, R., Omara, M., Zavala-Araiza, D., Maasakkers, J. D., Scarpelli, T. R., Lorente, A., Lyon, D., Sheng, J., Varon, D. J., Nesser, H., Qu, Z., Lu, X., Sulprizio, M. P., Hamburg, S. P., and Jacob, D. J.: Satellite quantification of oil and natural gas methane emissions in the US and Canada including contributions from individual basins, Atmospheric Chemistry and Physics, 22, 11203–11215, https://doi.org/10.5194/acp-22-11203-2022, 2022.

Soulie, A., Granier, C., Darras, S., Zilbermann, N., Doumbia, T., Guevara, M., Jalkanen, J.-P., Keita, S., Liousse, C., Crippa, M., Guizzardi, D., Hoesly, R., and Smith, S. J.: Global anthropogenic emissions (CAMS-GLOB-ANT) for the Copernicus Atmosphere Monitoring Service simulations of air quality forecasts and reanalyses, Earth System Science Data, 16, 2261–2279, https://doi.org/10.5194/essd-16-2261-2024, 2024.

Zavala-Araiza, D., Lyon, D., Alvarez, R. A., Palacios, V., Harriss, R., Lan, X., Talbot, R., and Hamburg, S. P.: Toward a Functional Definition of Methane Super-Emitters: Application to Natural Gas Production Sites, Environ. Sci. Technol., 49, 8167–8174, https://doi.org/10.1021/acs.est.5b00133, 2015.